

Geophysical Research Letters

RESEARCH LETTER

10.1029/2021GL093829

Key Points:

- Contributions of multiscale dynamic processes to the steric height (SH) in the SCS are revealed by 2-year moored temperature observations
- On average, mesoscales make the dominant contribution to SH, followed by tidal and supertidal motions, and finally submesoscales
- SHs of mesoscales and submesoscales are stronger in winter than summer but the opposite occurs for tidal and supertidal motions

Supporting Information:

Supporting Information may be found in the online version of this article.

Correspondence to:

Z. Zhang,
zzw330@ouc.edu.cn

Citation:

Miao, M., Zhang, Z., Qiu, B., Liu, Z., Zhang, X., Zhou, C., et al. (2021). On contributions of multiscale dynamic processes to the steric height in the northeastern South China Sea as revealed by moored observations. *Geophysical Research Letters*, 48, e2021GL093829. <https://doi.org/10.1029/2021GL093829>

Received 14 APR 2021

Accepted 25 JUN 2021

On Contributions of Multiscale Dynamic Processes to the Steric Height in the Northeastern South China Sea as Revealed by Moored Observations

Mingfang Miao¹ , Zhiwei Zhang^{1,2,3} , Bo Qiu⁴ , Zhiyu Liu⁵ , Xincheng Zhang¹, Chun Zhou^{1,2,3} , Shoude Guan^{1,2,3}, Xiaodong Huang^{1,2,3}, Wei Zhao^{1,2,3} , and Jiwei Tian^{1,2,3} 

¹Physical Oceanography Laboratory/IAOS and Frontiers Science Center for Deep Ocean Multispheres and Earth System, Ocean University of China, Qingdao, China, ²Pilot National Laboratory for Marine Science and Technology, Qingdao, China, ³Sanya Oceanographic Institution, Ocean University of China, Sanya, China, ⁴Department of Oceanography, University of Hawaii at Manoa, Honolulu, HI, USA, ⁵State Key Laboratory of Marine Environmental Science, Department of Physical Oceanography, College of Ocean and Earth Sciences, Xiamen University, Xiamen, China

Abstract Based on 2-year moored measurements in the northeastern South China Sea, contributions of multiscale dynamic processes to steric height (SH) at 60 m are quantified. It shows that on average, root-mean-squared (RMS) SHs of mesoscales, submesoscales, diurnal and semidiurnal internal tides (ITs), and supertidal internal gravity waves (IGWs) are 7.56, 1.01, 1.19, 2.84, and 1.46 cm, respectively, with their respective relative contributions of 53.8%, 7.2%, 8.5%, 20.2%, and 10.4%. The SHs of ITs and supertidal IGWs are dominated by stationary and nonstationary components, respectively. Seasonally, mesoscales and submesoscales show larger RMS SHs in winter than summer but the opposite occurs for ITs and supertidal IGWs. Although the RMS SH of submesoscales exceeds nonstationary ITs in winter, it is much smaller than the sum of nonstationary ITs and supertidal IGWs. Therefore, to detect submesoscales using SWOT data, approaches to remove the SHs of nonstationary ITs and supertidal IGWs are called for.

Plain Language Summary Steric height (SH) is a key component of sea surface height (SSH) that arises from multiscale processes such as mesoscales, submesoscales, and internal gravity waves (IGWs). A quantitative understanding on constituents of SH is a prerequisite to explore ocean dynamics using satellite-derived SSH data. Based on moored temperature data in the northeastern South China Sea, contributions of multiscale processes to SH are quantified. Two-year averaged results show that contributions of mesoscales, submesoscales, internal tides (ITs), and supertidal IGWs to SH account for 53.8%, 7.2%, 28.7%, and 10.4%, respectively. The SHs of ITs and supertidal IGWs are dominated by stationary and nonstationary components, respectively. The above multiscale processes all show notable seasonal variations in term of SH. For mesoscales and submesoscales (ITs and supertidal IGWs), their RMS SHs are larger (smaller) in winter than summer. In winter, the RMS SH of submesoscales reaches 1.26 cm, which exceeds the respective values of nonstationary ITs and supertidal IGWs, but is much smaller than their sum. These results suggest that in addition to nonstationary ITs, supertidal IGWs will also be a large “noise” source for detecting submesoscales from the upcoming SWOT SSH data.

1. Introduction

Sea surface height (SSH) is composed of a barotropic component associated with the mass of the water column and a baroclinic component arising from variations of water density. The baroclinic component of SSH is termed steric height (SH) and is related to the commonly used dynamic height by a factor of g (gravitational acceleration). In practice, the SH can be either computed using temperature/salinity (T/S) profiles or obtained through removing the atmospheric pressure loading and ocean bottom pressure from the observed SSH. Because variation of the SH can result from multiscale dynamic processes such as baroclinic Rossby and Kelvin waves, mesoscale to submesoscale fronts and eddies, as well as different types of internal gravity waves (IGWs), a quantitative knowledge of how these processes contribute to the SH is a prerequisite for exploring ocean dynamics from the SSH data (e.g., Baker-Yeboah et al., 2009; Gill & Niller, 1973; Guinehut et al., 2006).

Successful application of satellite altimetry-derived SSH in the past three decades since the launch of *T/P* in 1992 has resulted in a ground-breaking consensus that the world oceans are abundant with energetic mesoscale eddies, which have a typical horizontal scale of $O(50\text{--}500\text{ km})$ and account for the majority of the total kinetic energy (Ferrari & Wunsch, 2009; Fu et al., 2010; Klein et al., 2019). Before applying the altimeter-observed SSH to study mesoscale eddies and other quasi-geostrophic processes, one important step is to remove the barotropic part of SSH through corrections of inverted barometer and barotropic tides (AVISO, 2012). The remaining SSH after these corrections is predominantly SH (e.g., Wang et al., 2018). In addition to quasi-geostrophic processes, however, this SH-dominated SSH contains also nongeostrophic baroclinic signals associated with the internal tides (ITs) and other types of IGWs (Ray & Mitchum, 1996; Savage et al., 2017; Zhao et al., 2016). Because of the long repeat periods of altimeter satellites (several days to months), these IGW signals are aliased to longer periods and behave as a “noise” for studying mesoscale eddies. Whether these “noises” will lead to significant bias for mesoscale SSH depends on the relative SSH magnitude of mesoscale eddies and IGWs and remains to be evaluated using long-term high-frequency *in-situ* *T/S* measurements.

Although larger mesoscale eddies have been well studied by conventional nadir altimeters, due to their limited horizontal resolution (effective resolution of $\sim 150\text{ km}$; Fu et al., 2010), the nadir altimeters have missed signals of smaller mesoscale eddies with a horizontal scale of $50\text{--}150\text{ km}$ and submesoscale currents (hereafter submesoscales) with horizontal and time scales of $O(1\text{--}50\text{ km})$ and $O(1\text{--}10\text{ days})$, respectively. Given their importance in oceanic energy cascade and vertical tracer transports (Klein et al., 2019; McWilliams, 2016), the smaller mesoscales and submesoscales have become a key scientific target of the forthcoming Surface Water and Ocean Topography (SWOT) SAR-interferometry wide-swath altimeter mission, which will provide 7.5-km resolution SSH data with the root-mean-squared (RMS) noise of 0.36 cm in global ocean (Durand et al., 2010; Fu & Ubelmann, 2014; Morrow et al., 2019; Wang et al., 2019). Compared with mesoscale eddies, the submesoscales have a much smaller vertical scale (on order of 100 m) and correspondingly a much weaker SH (Qiu et al., 2018). As such, whether the noise level of SWOT measurements can meet the requirement to monitor submesoscales needs to be evaluated. In addition, because the spatiotemporal scales of IGWs (including ITs) are in general overlapped with submesoscales, their SSH signals will behave as large “noises” for identifying submesoscales from the SWOT data (Qiu et al., 2017; Rocha et al., 2016; Torres et al., 2018). Although the stationary component of ITs that is phase-locked to the astronomical tidal forcing can be removed using various techniques (e.g., harmonic analysis; Ray & Zaron, 2011; Zaron, 2015, 2017), the nonstationary ITs and supertidal IGWs are difficult to predict and remain a great challenge to the SWOT community (Arbic et al., 2018; Nelson et al., 2019; Savage et al., 2017). How “noisy” are the SSHs of nonstationary ITs and supertidal IGWs as compared with the submesoscales, whose strength tends to be stronger in winter than summer, also needs to be evaluated using long-term *in-situ* measurements.

The objective of this study is to evaluate the contributions of different dynamic processes, including mesoscale eddies, submesoscales, stationary and nonstationary ITs, and supertidal IGWs to the observed SH (equivalent to the steric SSH). Although similar evaluations have been done using high-resolution tidal-resolving numerical simulations (Qiu et al., 2018; Savage et al., 2017; Torres et al., 2018), the associated observational studies are rare due to the scarcity of long-term *T/S* data with both high vertical and temporal resolutions. In this study, the above objective is accomplished through quantifying the respective RMS SH of different dynamic processes based on 2-year moored temperature data in the northeastern South China Sea (NSCS). Existing observational and modeling studies suggest that the NSCS is abundant with strong ITs as well as complex mesoscale to submesoscale motions (Guan et al., 2014; Lin et al., 2020; Zhang et al., 2016, 2020; Zhao et al., 2016). As such, it is a good testbed to examine how feasible it is to adopt the future SWOT SSH data to quantitatively identify the quasi-geostrophically balanced smaller mesoscale eddies and larger submesoscales from a strong IGW background.

2. Data and Method

2.1. Moored Data

In order to calculate the SH, the 2-year long *T/S* chain data from the mooring SM1 (117.87°E , 21.12°N , depth $\sim 990\text{ m}$; Figure 1a) in the continental slope region of the NSCS were used. The SM1 is the central mooring

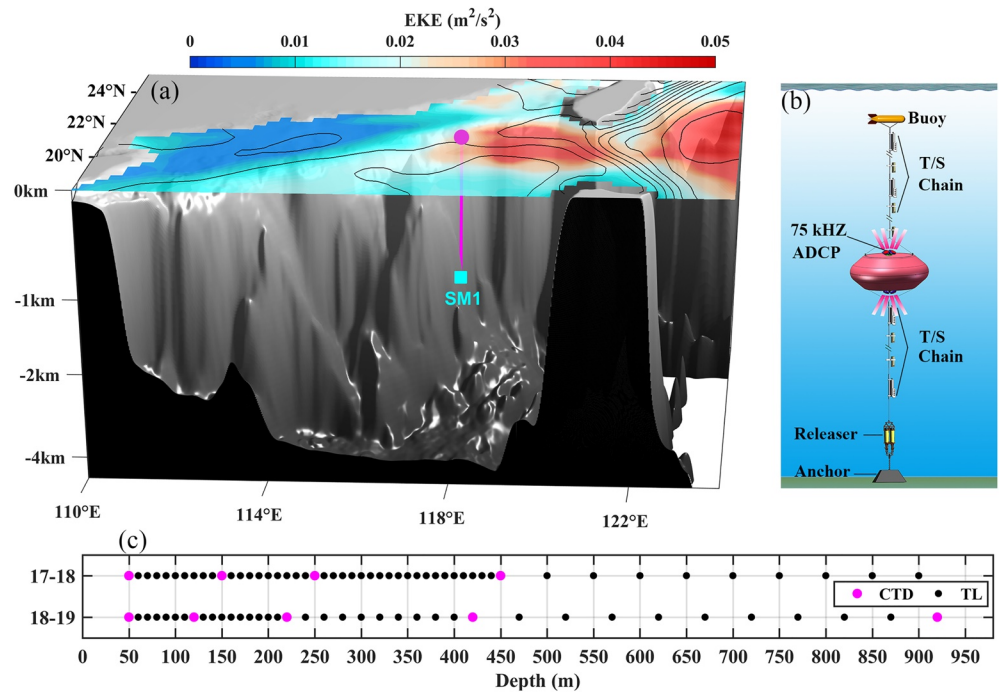


Figure 1. (a) Topography and the mooring location. Color shading and black contours at surface denote the altimeter-derived mean mesoscale eddy kinetic energy and sea surface height (SSH), respectively. Mooring location is indicated using purple dot and line. (b) Schematic diagram of the configuration of the mooring. Names of the instruments are marked in the diagram. (c) The designed depths of Conductivity-Temperature-Depths (CTDs; red dots) and temperature loggers (black dots) during the 2 years.

of the submesoscale-resolving mooring array in the SCS Mooring Array System, which was deployed from late June 2017 to late May 2018 (hereafter first period) and from early June 2018 to early July 2019 (hereafter second period) with an instrument replacement between the two periods (because the SHs from different moorings of the submesoscale array show very close results, only the SM1 mooring is analyzed here). To obtain long-term, continuous, high-resolution T/S measurements, the mooring was equipped with 46 temperature loggers (SBE56) and 4 CTDs (Conductivity-Temperature-Depths; SBE37) in the first period and 33 temperature loggers and 5 CTDs in the second period through nearly the entire water column. Temporal sampling intervals of CTDs and temperature loggers were all set as 3 min. Combination of the CTDs and temperature loggers provided us temperature data with vertical resolutions of 10 and 50 m between 50–450 and 450–900 m, respectively, for the first period, and 10, 20, and 50 m between 50–240, 240–420, and 420–920 m, respectively, for the second period. The mooring was also equipped with upward-looking and downward-looking 75 kHz acoustic Doppler current profilers (ADCPs). Detailed information of the mooring can be found in Figures 1b and 1c and Table S1.

After obtaining the temperature chain data, they were first linearly interpolated onto 5-m uniform vertical levels between ~ 50 and ~ 920 m (the precise vertical range depended on the instantaneous depths of the uppermost and lowermost CTDs) and then the data were averaged on an hourly basis. Due to the swing of the mooring caused by strong tidal and mesoscale currents (Figure S1), a portion of the temperature data were missing for several top layers. For a specific vertical level, if the proportion of missing data exceeded 50% of the total time length, this level was discarded for further analysis; on the other hand, the missing data were filled using linear interpolation if the missing proportion was $<50\%$.

2.2. Other Data Sets

To help evaluate relative errors of the moored data-based SH calculation, hourly T/S data of the llc4320 MITgcm output from September 13, 2011 to November 15, 2012 were used (Su et al., 2018). The llc4320 is

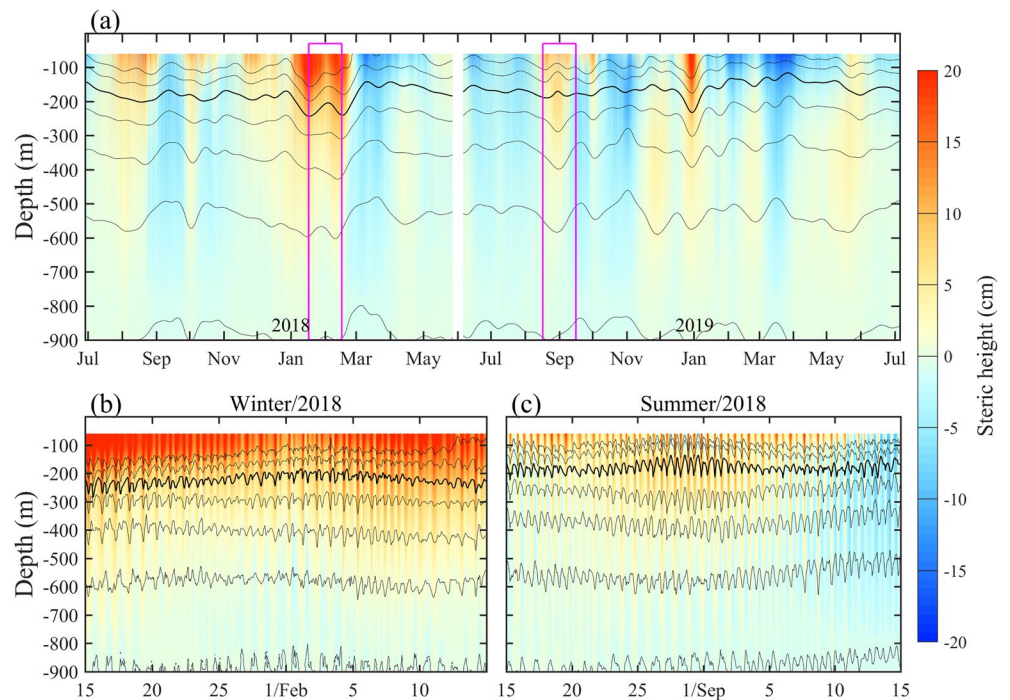


Figure 2. (a) Depth-time plots of the hourly steric height (SH). Black curves denote the 15-days low-pass filtered isotherms with a contour interval of 3 °C, for which the 17 °C isotherm is marked using thick line. (b, c) Zoom in on a winter month and a summer month marked by purple rectangles in (a), respectively. Isotherms in (b), (c) are the same as in (a) but plotted using hourly data.

a global ocean hydrostatic simulation, which is forced by 6-hourly ECMWF atmospheric forcing and the 16 major tidal constituents. The llc4320 output has 90 vertical levels and its horizontal resolution is $1/48^\circ$ (~ 2 km) that can partially resolve submesoscales (Qiu et al., 2018; Rocha et al., 2016; Su et al., 2018). Detailed model validations in the NSCS through comparison with observations can be found in Cao et al. (2019) and Lin et al. (2020). To better understand the mesoscale component of the SH, the multimission merged gridded altimeter sea level anomaly (SLA) data was used. Spatial and temporal resolutions of the SLA data are $1/4^\circ$ and 1 day, respectively. In addition, to obtain the T - S relations used in the density computation, the 1° monthly mean Argo T/S data from the International Pacific Research Center was also used in this study.

2.3. Calculation of Steric Height

By definition, the SH at level z referenced to level z_0 can be calculated as $\xi(z) = -\int_{z_0}^z \frac{\rho - \rho_0}{\rho_0} dz$, where ρ is the potential density and ρ_0 is its depth-time mean value. Here, ρ was computed based on moored temperature and salinity data using the MATLAB SeaWater toolbox (<http://www.cmar.csiro.au/datacentre/>). Note, however, that given the coarse resolution of the moored CTDs, the moored salinity was not directly used. Instead, salinity was reconstructed based on the moored temperature and the T - S relations derived through combining moored measurements and the IPRC Argo data. According to the effective coverage of the data, the maximum integral range in the formula is from -900 to -60 m (i.e., $z_0 = -900$ m and the shallowest z is -60 m; see Figure 2). In the following analysis, we focus primarily on ξ at 60-m depth except in Figure 2. Several factors such as interpolation of the missing data, coarse resolution of the temperature below 420 m, and usage of reconstructed salinity will result in potential errors in ξ . Through designing a virtual mooring using the llc4320 outputs, we found that these factors can cause a relative error of 18.4% (for details, see Supporting Information). To explore contributions of multiscale dynamic processes to ξ , we extracted its mesoscale, submesoscale, diurnal, semidiurnal, and supertidal components through band-pass filtering (fourth-order Butterworth) and then calculated corresponding RMS values. The cutoff periods of

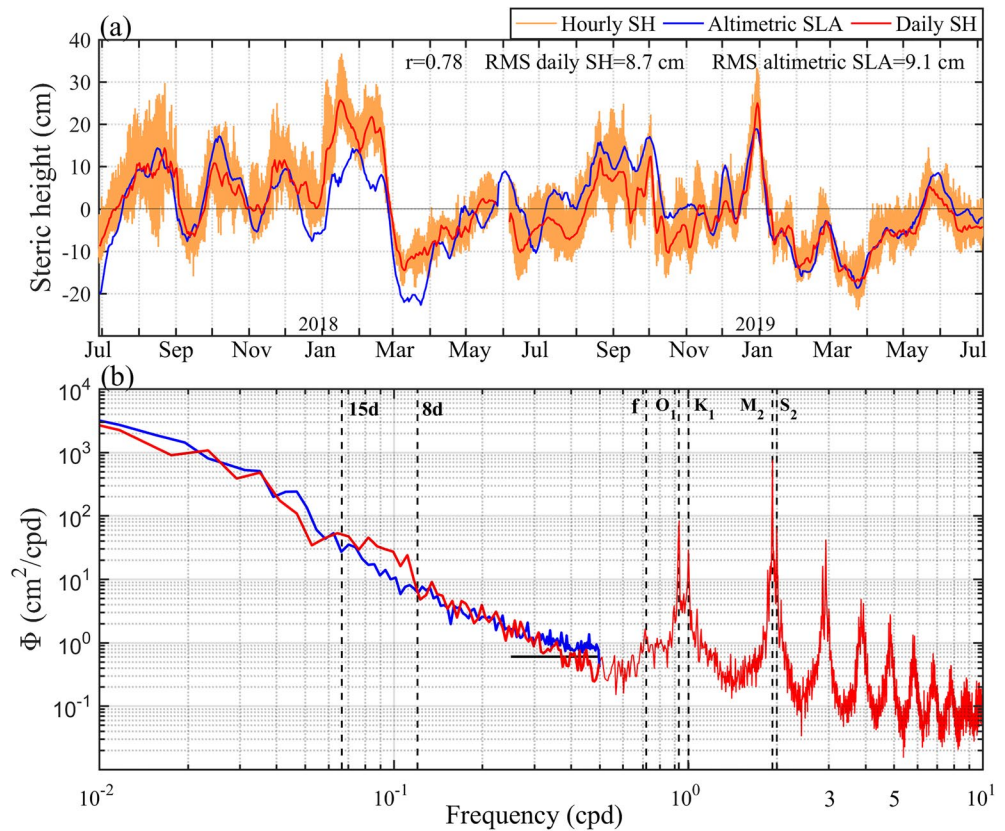


Figure 3. (a) Time series of the daily averaged steric height (SH) at 60 m (red) and altimetric sea level anomaly (SLA) (blue). The hourly SH is denoted using orange line. The respective root-mean-squared (RMS) values of SH and SLA as well as their correlation coefficient are marked. (b) Power spectral densities of the SH (red) and altimetric SLA (blue). Horizontal black line indicates the 0.25–0.5 cpd, where altimetric SLA shows nearly white noise.

the band-pass filtering for these multiscale components are set as 15–150 days, 2–15 days, 20–27 h, 10–14 h, and 4–10 h, respectively, following previous studies (e.g., Guan et al., 2014; Zhang et al., 2016, 2020, 2021).

3. Results

In Figure 2a, we show the depth-time plot of ξ during the whole observation period. Except for several special events such as the submesoscale coherent vortices in late August and late October 2018, ξ is overall surface intensified with a maximum magnitude exceeding 20 cm at 60-m depth (see also Figure 3a). The most prominent signals of ξ are concentrated in the period band of 15–150 days, which are primarily associated with propagating mesoscale eddies that cause strong thermocline heaving (or isotherm displacement). The mesoscale ξ is stronger in winter than summer, which well corresponds to the seasonality of eddy generations west of the Luzon Strait, the major origination region of eddies observed here (Li et al., 2015; Zhang et al., 2016, 2017). The second most prominent signals of ξ are due to semidiurnal and diurnal ITs, which become clearer if we zoom in on a specific month (Figures 2b and 2c). Similar to the mesoscale component, the semidiurnal and diurnal ξ are also surface intensified (Figure S2). Magnitude of the semidiurnal and diurnal ξ reaches several centimeters at 60-m depth.

In Figure 3a, we compare the time series of ξ at 60-m depth with the concurrent altimeter SLA (spatially interpolated onto the mooring site). For comparison, the time averages have been removed from the respective time series. The daily averaged ξ and SLA have a good agreement in both magnitude and temporal modulation. The RMS values of ξ and SLA are 8.7 and 9.1 cm, respectively, and their correlation reaches 0.78. This discrepancy is, however, understandable, as ξ is at 60-m depth (rather than the sea surface) and the mooring is on average 5 km away from the nearest track of altimetry satellites. It should be noticed that in

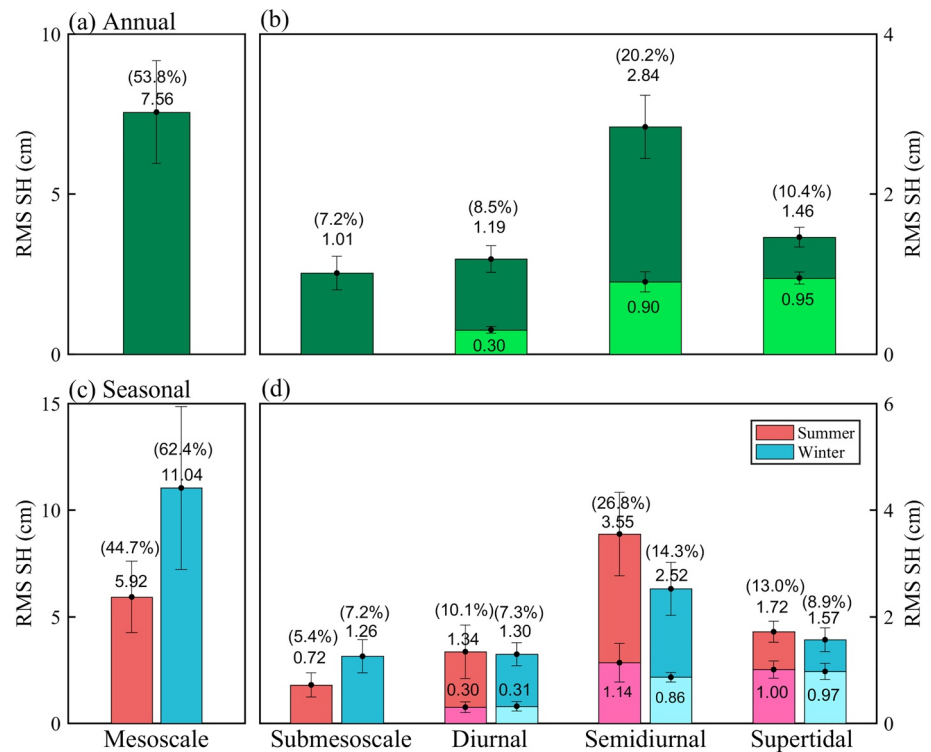


Figure 4. (a) Annual-mean results of the root-mean-squared (RMS) steric heights (SHs) at different frequency bands. The RMS value and its relative contribution to the total are marked. For the diurnal, semidiurnal, and supertidal bands, their nonstationary components are marked using light green shadings. Black vertical bars indicate the 95% confidence interval computed using bootstrap method. (b) Same as (a) but for the seasonal-mean results. Red and blue columns denote the RMS SHs in summer (June to August) and winter (December to February), respectively. The nonstationary components of diurnal and semidiurnal ITs and supertidal IGWs are marked using pink (light blue) shadings in summer (winter). Note that the minimum RMS SH of supertidal IGWs occurs in spring. That is, why its annual-mean result is smaller than that in both summer and winter.

contrast to the SLA, the daily ξ also shows small-amplitude fluctuations with periods shorter than 15 days that ride on the mesoscale signals. These short-period fluctuations are likely associated with submesoscales that cannot be resolved by the nadir altimeter data (Zhang et al., 2021).

To examine the variance of ξ at different time scales, its power spectral densities (PSD) are computed and shown in Figure 3b. The most prominent feature is the narrow large spectral peaks in the diurnal and semidiurnal bands corresponding to the O_1 , K_1 , M_2 , and S_2 ITs. In addition, spectral peaks in the subharmonic frequency bands (e.g., 3, 4, 5 cpd) are also evident, presumably generated through triad interactions among ITs of different frequencies (Guan et al., 2014). In contrast to the significant near-inertial peaks commonly found in the kinetic energy or velocity shear spectra (e.g., Guan et al., 2014; Zhang et al., 2018), there is no evident peaks in the near-inertial frequency band (0.7–0.9 cpd) in spectra of ξ . This is because near-inertial waves are dominated by horizontal motions with weak vertical isotherm displacements (Alford et al., 2016). Given that the RMS ξ of near-inertial waves is only 0.35 cm, they are not considered in our following analysis. In the subinertial frequency band, both ξ and SLA display red spectra with a similar shape and magnitude. Note that for frequencies below 1/15 cpd, the PSD of ξ are overall lower than the SLA but the opposite occurs for frequencies above 1/15 cpd, particularly between 1/15 and 1/8 cpd. The elevated ξ variance in this band corresponds to the submesoscale-like fluctuations in Figure 3a. These spectral features are similar to the velocity and vorticity spectra presented in Zhang et al. (2021), suggesting that a cutoff period of 15 days is reasonable to separate mesoscales and submesoscales.

In order to quantify contributions of multiscale dynamic processes to the SH variability, their respective RMS ξ was calculated based on the filtering scheme detailed in Section 2.3 (Figure 4). For the annual-mean result, RMS values of the mesoscale, submesoscale, diurnal, semidiurnal, and supertidal components of ξ

are 7.56, 1.01, 1.19, 2.84, and 1.46 cm, respectively, with their respective relative contributions being 53.8%, 7.2%, 8.5%, 20.2%, and 10.4%. For the supertidal ξ , >55% of it can be explained by the 2.5–3.5 cpd frequency band (Figure 3b). This means that although submesoscales make the smallest contribution to ξ , its RMS value is still much larger than the expected noise level of the 7.5 km SWOT SSH product (i.e., 0.36 cm). Based on the harmonic analysis, ξ of the stationary diurnal and semidiurnal ITs and supertidal IGWs (for subharmonic frequencies at 3, 4, 5 cpd, etc.) was calculated. For diurnal and semidiurnal ITs, ξ is dominated by the stationary components with their respective proportion of 74.8% and 68.3%. With respect to the supertidal ξ , however, its stationary component only accounts for 34.9%. After removing ξ of the stationary components, the RMS values of the remaining (nonstationary) ξ of diurnal and semidiurnal ITs and supertidal IGWs still reach 0.30, 0.90, and 0.95 cm, respectively. The sum of these nonstationary ξ (particularly for semidiurnal and supertidal ones), which is difficult to predict and remove, far exceeds the submesoscale ξ . Therefore, they will pose as a large “noise” source for the SWOT mission to observe submesoscales in the NSCS.

In Figure 4b, RMS ξ values of multiscale processes in summer and winter seasons are compared. Here, the summer and winter seasons are defined as June to August and December to February, respectively. It shows that both mesoscales and submesoscales show much larger ξ in winter than summer. The seasonality of mesoscale ξ here is closely associated with the mesoscale eddies west of the Luzon Strait, which are more frequently generated in winter due to the stronger Kuroshio intrusion and the associated barotropic and baroclinic instabilities (Li et al., 2015; Wang et al., 2020; Zhang et al., 2017). The enhanced submesoscale ξ in winter can be ascribed to the stronger mesoscale strain and deeper mixed-layer depth, which provide favorable conditions for the generation of submesoscales through eddy-induced frontogenesis and mixed-layer instability (Zhang et al., 2020, 2021). In contrast to mesoscales and submesoscales, ξ in the IGWs band, particularly for semidiurnal ITs and supertidal IGWs, shows the opposite seasonality. Enhanced IGWs ξ in summer is mainly due to stronger stratification and a shallower pycnocline (Lin et al., 2020). In summer, RMS ξ of submesoscales (i.e., 0.72 cm) is smaller than supertidal IGWs as well as nonstationary ITs (the sum of the diurnal and semidiurnal components). In winter, the RMS ξ of submesoscales reaches 1.26 cm, which exceeds the respective values of nonstationary ITs (i.e., 1.17 cm) and nonstationary supertidal IGWs (i.e., 0.97 cm) but is still much smaller than their sum (i.e., 2.14 cm). This situation cannot be reversed even if the underestimation of submesoscale ξ due to the absent upper-60 m data is revised (22.9% underestimation according to Table S2). These results suggest that even in winter, the large ξ of nonstationary ITs and supertidal IGWs (particularly the semidiurnal ITs and the 3 cpd subharmonic waves) is still a large “noise” source for SWOT to detect submesoscales in the NSCS.

4. Summary and Discussion

Based on 2-year long moored temperature data in the NSCS, contributions of multiscale dynamic processes (including mesoscales, submesoscales, ITs, and supertidal IGWs) to the SH are quantified. The results show that on average, mesoscales make the dominant contribution to the SH, followed by semidiurnal IT, then supertidal IGWs, diurnal IT, and finally submesoscales. The annual-mean RMS ξ (i.e., the SH at 60-m depth) values of these processes are 7.56, 2.84, 1.46, 1.19, and 1.01 cm, respectively, with their respective relative contributions of 53.8%, 20.2%, 10.4%, 8.5%, and 7.2%. Note that due to the data absence in the upper 60 m, the RMS SHs of these processes have been underestimated by 16.3%, 7.2%, 10.9%, 15.1%, and 22.9%, respectively (Table S2). For the diurnal and semidiurnal ITs, ~70% of their ξ is caused by the stationary component, which therefore is predictable and can to a large degree be removed. With respect to the supertidal IGWs, however, it is dominated by the nonstationary component with the proportion as high as 65.1%. The ADCP measurements show that magnitude of the quasi-geostrophic balanced velocity (thus pressure anomaly) near the bottom is one order of magnitude smaller than that near the surface (Figure S3). This suggests that for the balanced motions, the SH can to a large degree represent the SSH here, which agrees with recent observations that the RMS barotropic SSH is only several millimeters in our study region (Zhao et al., 2017; Zheng et al., 2021).

The SHs of the multiscale dynamic processes all show notable seasonal variabilities. Both the mesoscale and submesoscale ξ is larger in winter than summer while the opposite occurs for IGWs (including ITs). In summer, RMS ξ of submesoscales is much smaller than nonstationary ITs and also nonstationary supertidal IGWs. In winter, the RMS ξ of submesoscales reaches 1.26 cm, which is 75% larger than that in summer.

Although the wintertime RMS ξ of submesoscales exceeds the respective values of nonstationary ITs and supertidal IGWs, it is still much smaller than the sum of the latter (1.26 versus 2.14 cm). These results suggest that in addition to the well-recognized nonstationary ITs, the supertidal IGWs that are dominated by nonstationary components will be an equally important noise source for detecting submesoscales in the NSCS based on the SWOT data.

Given that the NSCS is a near-source region of strong ITs and its geostrophic energy level is moderate, the relative contributions of multiscale dynamic processes reported here may not be representative for the regions with energetic geostrophic flows (such as the Kuroshio Extension and the Antarctic Circumpolar Current) that have high signal-to-noise ratios for submesoscales. However, in the broad low or moderate geostrophic flow regions in open ocean, even though the ITs are relatively weak, the supertidal IGWs may also cause considerable SH noise. For example, moored T/S measurements in the North Pacific Subtropical Countercurrent region (with both moderate geostrophic energy and ITs; Zhang et al., 2021) indicate that the RMS ξ of supertidal IGWs is comparable in magnitude with submesoscales (not shown). Therefore, how to remove supertidal IGWs from the future SWOT SSH is a challenge for the submesoscale community. Finally, it deserves to point out that compared with the moored observations, the llc4320 simulation has underestimated the submesoscale ξ but overestimated that of ITs and IGWs (Figure S4). This simulation bias should be considered when using the llc4320 output to design the SWOT calibration/validation experiment or evaluate the transition scale from balanced to unbalanced motions (e.g., Qiu et al., 2018; Wang et al., 2018).

Data Availability Statement

The llc4320 MITgcm output is available at <https://data.nas.nasa.gov/ecco/data.php>. The llc4320 data extraction by Dr. Dimitris Menemenlis are appreciated. The altimeter SLA data were obtained from https://resources.marine.copernicus.eu/?option=com_csw&view=details&product_id=SEALEVEL_GLO_PHY_L4_REP_OBSERVATIONS_008_047. The Argo data were downloaded from <http://apdrc.soest.hawaii.edu/las/v6/dataset?catitem=201>. The analyzed moored data are available at Harvard Dataverse via <https://doi.org/10.7910/DVN/YREGWO>.

Acknowledgments

This study was jointly supported by the National Natural Science Foundation of China (NSFC; 42076004, 41706005, 91958205, 91858203), the National Key Research and Development Program of China (NRDP; 2018YFA0605702, 2016YFC1402605), and the Fundamental Research Funds for the Central Universities (202041009, 201861006, 202013028). Z. Liu was supported by the NSFC (41622601, 91858201) and the NRDP (2016YFC1401404).

References

- Alford, M. H., MacKinnon, J. A., Simmons, H. L., & Nash, J. D. (2016). Near-inertial internal gravity waves in the ocean. *Annual Review of Marine Science*, 8, 95–123.
- Arbic, B., Alford, M. H., Ansong, J. K., Buijsman, M. C., Ciotti, R. B., Farrar, J., et al. (2018). A primer on global IT and internal gravity wave continuum modeling in HyCOM and MITgcm. In E. Chassignet, A. Pascual, J. Tintore, & J. Verron (Eds.), *New Frontiers in operational oceanography* (pp. 307–391). Tallahassee, FL: GODAE OceanView. <https://doi.org/10.17125/gov2018.ch13>
- AVISO. (2012). *DT CorSSH and DT SLA product handbook* (p. 17). AVISO Altimetry. Retrieved from http://www.aviso.altimetry.fr/fileadmin/documents/data/tools/hdbk_dt_corssh_dt_sla.pdf
- Baker-Yeboah, S., Watts, D. R., & Byrne, D. A. (2009). Measurements of sea surface height variability in the eastern Atlantic from pressure sensor-equipped inverted echo sounders: Baroclinic and barotropic components. *Journal of Atmospheric and Oceanic Technology*, 26, 2593–2609. <https://doi.org/10.1175/2009JTECHO659.1>
- Cao, H., Jing, Z., Fox-Kemper, B., Yan, T., & Qi, Y. (2019). Scale transition from geostrophic motions to internal waves in the northern South China Sea. *Journal of Geophysical Research: Oceans*, 124, 9364–9383. <https://doi.org/10.1029/2019JC015575>
- Durand, M., Fu, L.-L., Lettenmaier, D. P., Alsdorf, D. E., Rodríguez, E., & Esteban-Fernandez, D. (2010). The surface water and ocean topography mission: Observing terrestrial surface water and oceanic submesoscale eddies. *Proceedings of the IEEE*, 98, 766–779. <https://doi.org/10.1109/JPROC.2010.2043031>
- Ferrari, R., & Wunsch, C. (2009). Ocean circulation kinetic energy: Reservoirs, sources, and sinks. *Annual Review of Fluid Mechanics*, 41, 253–282.
- Fu, L.-L., Chelton, D. B., Le Traon, P.-Y., & Morrow, R. (2010). Eddy dynamics from satellite Altimetry. *Oceanography*, 23(4), 14–25. <https://doi.org/10.5670/oceanog.2010.02>
- Fu, L.-L., & Ubelmann, C. (2014). On the transition from profile altimeter to swath altimeter for observing global ocean surface topography. *Journal of Atmospheric and Oceanic Technology*, 31, 560–568. <https://doi.org/10.1175/JTECH-D-13-00109.1>
- Gill, A. E., & Niller, P. P. (1973). The theory of the seasonal variability of the ocean. *Deep Sea Research and Oceanographic Abstracts*, 20, 141–177.
- Guan, S., Zhao, W., Huthnance, J., Tian, J., & Wang, J. (2014). Observed upper ocean response to typhoon Megi (2010) in the Northern South China Sea. *Journal of Geophysical Research: Oceans*, 119, 3134–3157. <https://doi.org/10.1002/2013JC009661>
- Guinehut, S., Le Traon, P.-Y., & Larnicol, G. (2006). What can we learn from global altimetry/hydrography comparisons? *Geophysical Research Letters*, 33, L10604. <https://doi.org/10.1029/2005GL025551>
- Klein, P., Lapeyre, G., Siegelman, L., Qiu, B., Fu, L.-L., Torres, H., et al. (2019). Ocean-scale interactions from space. *Earth and Space Science*, 6, 795–817. <https://doi.org/10.1029/2018EA000492>
- Li, C., Zhang, Z., Zhao, W., & Tian, J. (2015). Temporal variability of the current in the northeastern South China Sea revealed by 2.5-year-long moored observations. *Journal of Oceanography*, 71(4), 361–372.

- Lin, H., Liu, Z., Hu, J., Menemenlis, D., & Huang, Y. (2020). Characterizing meso- to submesoscale features in the South China Sea. *Progress in Oceanography*, 188, 102420. <https://doi.org/10.1016/j.pocean.2020.102420>
- McWilliams, J. C. (2016). Submesoscale currents in the ocean. *Proceedings of the Royal Society*, A472, 20160117.
- Morrow, R., Fu, L.-L., Arduin, F., Benkiran, M., Chapron, B., Cosme, E., et al. (2019). Global observations of fine-scale ocean surface topography with the surface water and ocean topography (SWOT) mission. *Frontier in Marine Science*, 6, 1–19.
- Nelson, A. D., Arbic, B. K., Zaron, E. D., Savage, A. C., Richman, J. G., Buijsman, M. C., & Shriver, J. F. (2019). Toward realistic nonstationarity of semidiurnal baroclinic tides in a hydrodynamic model. *Journal of Geophysical Research: Oceans*, 124, 6632–6642. <https://doi.org/10.1029/2018JC014737>
- Qiu, B., Chen, S., Klein, P., Wang, J., Torres, H., Fu, L.-L., & Menemenlis, D. (2018). Seasonality in transition scale from balanced to unbalanced motions in the world ocean. *Journal of Physical Oceanography*, 48, 591–605.
- Qiu, B., Nakano, T., Chen, S., & Klein, P. (2017). Submesoscale transition from geostrophic flows to internal waves in the northwestern Pacific upper ocean. *Nature Communication*, 8, 14055. <https://doi.org/10.1038/ncomms14055>
- Ray, R. D., & Mitchum, G. T. (1996). Surface manifestation of ITs generated near Hawaii. *Geophysical Research Letters*, 23(16), 2101–2104. <https://doi.org/10.1029/96GL02050>
- Ray, R. D., & Zaron, E. D. (2011). Non-stationary ITs observed with satellite altimetry. *Geophysical Research Letters*, 38, L17609. <https://doi.org/10.1029/2011GL048617>
- Rocha, C. B., Gille, S. T., Chereskin, T. K., & Menemenlis, D. (2016). Seasonality of submesoscale dynamics in the Kuroshio Extension. *Geophysical Research Letters*, 43, 11304–11311. <https://doi.org/10.1002/2016GL071349>
- Savage, A. C., Arbic, B. K., Richman, J. G., Shriver, J. F., Alford, M. H., Buijsman, M. C., et al. (2017). Frequency content of sea surface height variability from internal gravity waves to mesoscale eddies. *Journal of Geophysical Research: Oceans*, 122, 2519–2538. <https://doi.org/10.1002/2016JC012331>
- Su, Z., Wang, J., Klein, P., Thompson, A. F., & Menemenlis, D. (2018). Ocean submesoscales as a key component of the global heat budget. *Nature Communications*, 9, 775. <https://doi.org/10.1038/s41467-018-02983-w>
- Torres, H. S., Klein, P., Menemenlis, D., Qiu, B., Su, Z., Wang, J., et al. (2018). Partitioning ocean motions into balanced motions and internal gravity waves: A modeling study in anticipation of future space missions. *Journal of Geophysical Research: Oceans*, 123, 8084–8105. <https://doi.org/10.1029/2018JC014438>
- Wang, J., Fu, L.-L., Qiu, B., Menemenlis, D., Farrar, J. T., Chao, Y., et al. (2018). An observing system simulation experiment for the calibration and validation of the surface water ocean topography sea surface height measurement using in situ platforms. *Journal of Atmospheric and Oceanic Technology*, 35, 281–297. <https://doi.org/10.1175/JTECH-D-17-0076.1>
- Wang, J., Fu, L.-L., Torres, H. S., Chen, S., Qiu, B., & Menemenlis, D. (2019). On the spatial scales to be resolved by the surface water and ocean topography Ka-band radar interferometer. *Journal of Atmospheric and Oceanic Technology*, 36(1), 87–99.
- Wang, Q., Zhou, W., Zeng, L., Chen, J., He, Y., & Wang, D. (2020). Intraseasonal variability of cross-slope flow in the northern South China Sea. *Journal of Physical Oceanography*, 50, 2071–2084. <https://doi.org/10.1175/JPO-D-19-0293.1>
- Zaron, E. D. (2015). Non-stationary ITs inferred from dual-satellite altimetry. *Journal of Physical Oceanography*, 45(9), 2239–2246. <https://doi.org/10.1175/JPO-D-15-0020.1>
- Zaron, E. D. (2017). Mapping the nonstationary IT with satellite altimetry. *Journal of Geophysical Research: Oceans*, 122, 539–554. <https://doi.org/10.1002/2016JC012487>
- Zhang, Z.-W., Qiu, B., Tian, J., Zhao, W., & Huang, X. (2018). Latitude-dependent finescale turbulent shear generations in the Pacific tropical-extratropical upper ocean. *Nature Communication*, 9, 4086. <https://doi.org/10.1038/s41467-018-06260-8>
- Zhang, Z.-W., Tian, J., Qiu, B., Zhao, W., Chang, P., Wu, D., & Wan, X. (2016). Observed 3D structure, generation, and dissipation of oceanic mesoscale eddies in the South China Sea. *Scientific Reports*, 6, 24349. <https://doi.org/10.1038/srep24349>
- Zhang, Z.-W., Zhang, X., Qiu, B., Zhao, W., Zhou, C., Huang, X., & Tian, J. (2021). Submesoscale currents in the subtropical upper ocean observed by long-term high-resolution mooring arrays. *Journal of Physical Oceanography*, 51(1), 187–206. <https://doi.org/10.1175/JPO-D-20-0100.1>
- Zhang, Z.-W., Zhang, Y., Qiu, B., Sasaki, H., Sun, Z., Zhang, X., et al. (2020). Spatiotemporal characteristics and generation mechanisms of submesoscale currents in the northeastern South China Sea revealed by numerical simulations. *Journal of Geophysical Research: Oceans*, 125, e2019JC015404. <https://doi.org/10.1029/2019JC015404>
- Zhang, Z.-W., Zhao, W., Qiu, B., & Tian, J. (2017). Anticyclonic eddy sheddings from Kuroshio loop and the accompanying cyclonic eddy in the northeastern South China Sea. *Journal of Physical Oceanography*, 47(6), 1243–1259.
- Zhao, R., Zhu, X.-H., & Guo, X. (2017). The impact of monsoon winds and mesoscale eddies on thermohaline structures and circulation patterns in the northern South China Sea. *Continental Shelf Research*, 143, 240–256.
- Zhao, Z., Alford, M. H., Garton, J., Rainville, L., & Simmons, H. (2016). Global observations of open-ocean mode-1 M_2 ITs. *Journal of Physical Oceanography*, 46, 1657–1684. <https://doi.org/10.1175/JPO-D-15-0105.1>
- Zheng, H., Zhang, C., Zhao, R., Zhu, X.-H., Zhu, Z.-N., Liu, Z.-J., & Wang, M. (2021). Structure and variability of abyssal current in northern South China Sea based on CRIES observations. *Journal of Geophysical Research: Oceans*, 126, e2020JC016780. <https://doi.org/10.1029/2020JC016780>